

Review

Open Access

Phase microscopy and surface profilometry by digital holography

Myung K. Kim* 

Abstract

Quantitative phase microscopy by digital holography is a good candidate for high-speed, high precision profilometry. Multi-wavelength optical phase unwrapping avoids difficulties of numerical unwrapping methods, and can generate surface topographic images with large axial range and high axial resolution. But the large axial range is accompanied by proportionately large noise. An iterative process utilizing holograms acquired with a series of wavelengths is shown to be effective in reducing the noise to a few micrometers even over the axial range of several millimeters. An alternate approach with shifting of illumination angle, instead of using multiple laser sources, provides multiple effective wavelengths from a single laser, greatly simplifying the system complexity and providing great flexibility in the wavelength selection. Experiments are performed demonstrating the basic processes of multi-wavelength digital holography (MWDH) and multi-angle digital holography (MADH). Example images are presented for surface profiles of various types of surface structures. The methods have potential for versatile, high performance surface profilometry, with compact optical system and straightforward processing algorithms.

Keywords: Phase, Microscopy, Profilometry, Digital, Holography

Introduction

Surface profilometry is an essential technology in many fields of industry such as micro-electronics fabrication and precision machining, as well as in biomedicine. Traditional mechanical stylus-based scanners are largely replaced by non-contact optical methods, such as using patterned illumination, multi-view triangulation, and white light interference¹. Digital holography is a new candidate for high speed, high precision profilometry, due to its ability to reconstruct both the amplitude and the phase of the full optical field. The phase profile of the hologram is directly proportional to the optical path length, such as from transmission through the thickness of a material or reflection off a surface². This is the basis of many applications of quantitative phase microscopy by digital

holography, such as cellular microscopy^{3,4}, micro-device diagnostics⁵, and microfluidics⁶, to name a few.

The complex, i.e. amplitude and phase, field profile is extracted from the interference intensity patterns by off-axis or phase-shifting digital holography⁷. The optical phase is proportional to the optical path length, but only up to modulo 2π , and therefore the measured optical path length is ambiguous modulo one wavelength. The so-called phase unwrapping is a common problem in any phase imaging systems, and many numerical phase unwrapping algorithms have been developed⁸, which are typically based on subjective decisions regarding locations of phase discontinuity, and tend to be non-deterministic, unpredictable, and computationally heavy. A technique called optical phase unwrapping has been introduced^{9–11}, based on combination of several holograms acquired with different wavelengths, that generates phase profiles with

Correspondence: Myung K. Kim (mkkim@usf.edu)
Department of Physics, University of South Florida, Tampa, FL 33620

© The Author(s) 2022



Open Access This article is licensed under a Creative Commons Attribution 4.0 International License, which permits use, sharing, adaptation, distribution and reproduction in any medium or format, as long as you give appropriate credit to the original author(s) and the source, provide a link to the Creative Commons license, and indicate if changes were made. The images or other third party material in this article are included in the article's Creative Commons license, unless indicated otherwise in a credit line to the material. If material is not included in the article's Creative Commons license and your intended use is not permitted by statutory regulation or exceeds the permitted use, you will need to obtain permission directly from the copyright holder. To view a copy of this license, visit <http://creativecommons.org/licenses/by/4.0/>.

effective wavelength¹² much larger than the original wavelengths. The method is completely deterministic and computationally straightforward, and works well even when phase topology is complicated.

The effective, or synthetic, wavelength can be made very large by choosing two closely spaced wavelengths, but this entails proportionate amplification of any noise in the resulting optical path profile. It then becomes necessary to acquire and combine additional holograms with a third, fourth, or more wavelengths, and the noise is reduced in an iterative process described below. The larger the height range to be measured or the more severe the noise level, the more number of wavelengths and holograms is required. The multi-wavelength digital holography (MWDH) has been proposed and demonstrated using a dye laser tuned at three different wavelengths¹³, a tunable diode laser at seven different wavelengths¹⁴, or three discrete lasers¹⁵, for example.

But the use of more than two or three wavelengths becomes increasingly difficult because of the complexity and cost of the optical system, as well as possible chromatic aberration over large range of wavelengths¹⁶. On the other hand, it has been noted early on that a shift in object illumination angle can also have a similar effect as a wavelength shift, because of the variation in the optical path length through a given height or thickness of the object¹⁷. Instead of a set of multiple lasers or scanning of a tunable laser, the angular direction of illumination is scanned to multiple positions to achieve essentially the same effect as with multiple wavelengths.

This article reports a series of studies on optical phase unwrapping based on multi-wavelength digital holography (MWDH) or multi-angle digital holography (MADH) for potential applications in surface profiling with millimeter-scale axial range and micrometer-range axial resolution. In MWDH studies, up to four wavelengths, from as many discrete lasers, are used to generate surface profiles with several mm height range and several μm height resolution. In MADH studies, it is possible to apply as many as eight different effective wavelengths with a much simpler and flexible optical system. The experimental results are summarized in Section 2. Discussions in Section 3 include comparison of the MWDH and MADH systems. These systems are also described in comparison with a few other related but distinct systems that utilize multi-wavelength or multi-angle acquisition of holograms. Section 4 describes the theoretical background and experimental system and processes.

Results

For illustration of basic processes of four-wavelength

MWDH in Fig. 1, the object consists of a pair of glass plates with resolution target patterns with the step size between them measured to be 1.54 mm. As detailed in Materials and Methods, a set of four holograms are acquired by phase-shifting digital holography using four lasers with wavelengths $\lambda_1 = 0.639\,616\,\mu\text{m}$, $\lambda_2 = 0.639\,595\,\mu\text{m}$, $\lambda_3 = 0.639\,539\,\mu\text{m}$, and $\lambda_4 = 0.638\,929\,\mu\text{m}$. Fig. 1a, b display the first two phase profiles $\Phi_1(x, y)$ and $\Phi_2(x, y)$. Because of the minute difference of $0.000\,025\,\mu\text{m}$ between the two wavelengths, any difference between the two phase profiles is not easily discernable. Take the difference between the two phase profiles, modulo 2π , and rescale with the synthetic wavelength $\Lambda_{12} = \lambda_1\lambda_2/|\lambda_1 - \lambda_2|$, to obtain the height profile Z_{12} . The three-dimensional shape of the object then becomes apparent, shown in Fig. 1c, as well as the step between the two glass plates in Fig. 2a. The set of parameters used in this experiment is tabulated in Table 1.

The difference of the two phase profiles corresponds to another phase profile with very large synthetic wavelength $\Lambda_{12} = 19\,749\,\mu\text{m}$, amplifying the wavelength by a factor of $\Lambda_{12}/\lambda_1 \approx 3 \times 10^4$. The difference phase map has the same level of phase noise, other than a factor of order one, as the initial phase maps, meaning that with the amplification of effective wavelength, the noise in the height profile is also amplified by the same factor. In Fig. 2a, the noise in the height profile is measured to be $\delta Z_{12} = 919.1\,\mu\text{m}$, and the 3D profile in Fig. 1c shows significant amount of rough and spiky textures on the surfaces. Significant reduction in noise is achieved by iterative stitching of additional difference phase profiles Z_{13} and Z_{14} with shorter synthetic wavelengths $\Lambda_{13} = 5\,302\,\mu\text{m}$ and $\Lambda_{14} = 595\,\mu\text{m}$, respectively. The stitching process maintains the overall height range to Λ_{12} while reducing the noise to the

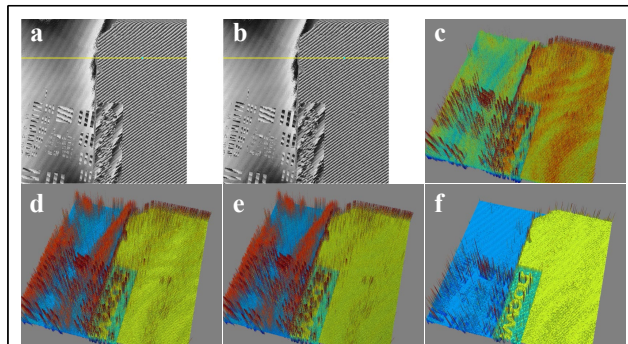


Fig. 1 Basic process of optical phase unwrapping by MWDH using four wavelengths, tabulated in Table 1. The object is a stack of two resolution target surfaces, with field of view $24 \times 24\text{ mm}^2$. **a** $\Phi_1(x, y)$; **b** $\Phi_2(x, y)$; **c** $Z_{12}(x, y)$; **d** $Z_{12 \dots 3}(x, y)$; **e** $Z_{12 \dots 4}(x, y)$; **f** $Z_{\text{proc}}(x, y)$. See Fig. 2 for indication of the z-scale. See text for details.

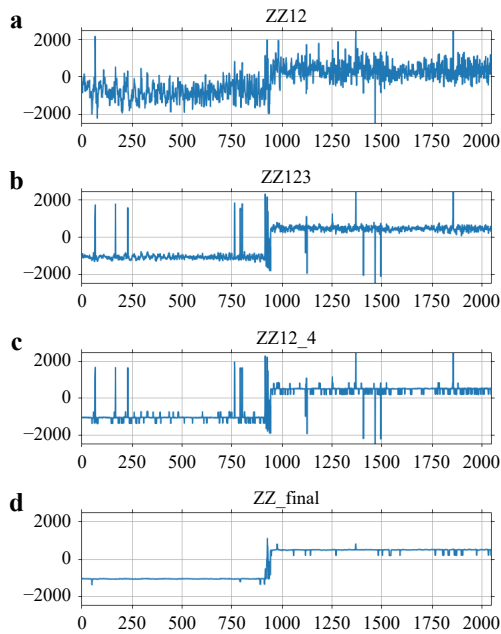


Fig. 2 Graphs of cross-sections of **a** Z_{12} ; **b** $Z_{12...3}$; **c** $Z_{12...4}$; **d** Z_{proc} , through the yellow line indicated in Fig. 1a. The vertical scales, in μm , are multiplied by a factor 0.5 to account for the reflection geometry. The horizontal scale is the pixel index. A 3×3 median filter is applied to $Z_{12...4}$ to obtain Z_{proc} . Measured height noise is tabulated in Table 1. The measured step height is 1.55 mm, comparable to the 1.54 mm nominal glass thickness.

Table 1 Parameter used in Fig. 1. λ_n : individual wavelength; Δ_{1n} : difference wavelength; Λ_{1n} : synthetic wavelength; δZ_{1n} : noise in Z_{1n} ; 'proc': final processed profile.

n	$\lambda_n, \mu\text{m}$	$\Delta_{1n}, \mu\text{m}$	$\Lambda_{1n}, \mu\text{m}$	$\delta Z_{1n}, \mu\text{m}$
1	0.639 616			
2	0.639 595	0.000 021	19 749.176	919.138
3	0.639 539	0.000 077	5 301.693	564.925
4	0.638 929	0.000 687	594.695	593.199
proc				101.721

proportionately lower levels of Z_{13} and Z_{14} , whose measured noise in Fig. 2d, e are $\delta Z_{13} = 564.9 \mu\text{m}$ and $\delta Z_{14} = 593.2 \mu\text{m}$, respectively. The last stitching operation with Z_{14} has no apparent improvement in the measured noise because the reduction in synthetic wavelength is too rapid. The necessary condition is given in the Materials and Methods section, but with the given set of laser wavelengths, there is no flexibility in the choice of wavelengths. On the other hand, as we will see, the generation of effective wavelength can be made very flexible by varying the object illumination angle instead. A common and effective method of reducing spiky noise is using median filters. A mild median filter with 3×3 window is applied to the last

profile $Z_{12...4}$ of the iterative series to obtain the final processed profile Z_{proc} in Fig. 1f and Fig. 2d, where the corresponding noise is reduced to $\delta Z_{proc} = 101.7 \mu\text{m}$. The measured step height in Z_{proc} is 1.55 mm, consistent with the nominal thickness of the glass plate.

In Fig. 3, 4, a similar set of parameters is used to image the surface of a US quarter dollar coin, placed on a mirror-

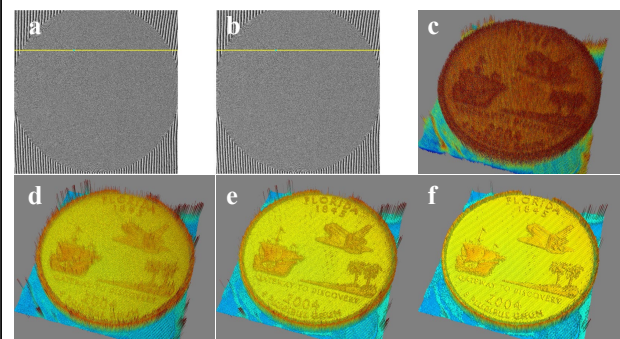


Fig. 3 Example of optical phase unwrapping by MWDH. The object is a US quarter dollar coin, with field of view $24 \times 24 \text{ mm}^2$. A set of four wavelengths are used, such that $\Lambda_{12} = 28\,213 \mu\text{m}$, $\Lambda_{13} = 4\,328 \mu\text{m}$, and $\Lambda_{14} = 485 \mu\text{m}$. **a** $\Phi_1(x, y)$; **b** $\Phi_2(x, y)$; **c** $Z_{12}(x, y)$; **d** $Z_{12...3}(x, y)$; **e** $Z_{12...4}(x, y)$; **f** $Z_{proc}(x, y)$. See Fig. 4 for indication of the z-scale.

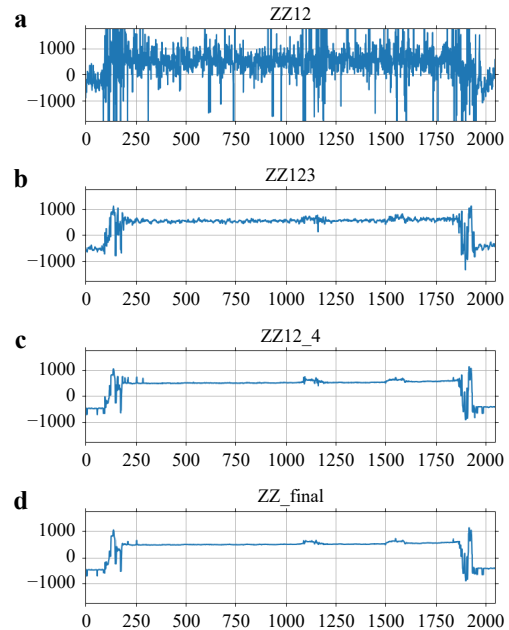


Fig. 4 Graphs of cross-sections of **a** Z_{12} ; **b** $Z_{12...3}$; **c** $Z_{12...4}$; **d** Z_{proc} , through the yellow line indicated in Fig. 3a. The vertical scales, in μm , are multiplied by a factor 0.5 to account for the reflection geometry. The horizontal scale is the pixel index. A 3×3 median filter is applied to each of $Z_{12} \sim Z_{12...4}$ and to Z_{proc} . Measured height noise varies as $\delta Z_{12} = 385.0 \mu\text{m}$, $\delta Z_{12...3} = 22.6 \mu\text{m}$, $\delta Z_{12...4} = 3.8 \mu\text{m}$, and $\delta Z_{proc} = 3.2 \mu\text{m}$.

like surface. The synthetic wavelengths used were $\Lambda_{12} = 28\,213\,\mu\text{m}$, $\Lambda_{13} = 5\,302\,\mu\text{m}$, $\Lambda_{14} = 595\,\mu\text{m}$. The single-wavelength phase profiles in Fig. 3a, b have no discernable features, because of the random granular structure of the metallic surface. Yet the surface profile Z_{12} from the difference profile does reveal the overall features of the surface pattern. The iterative processing with ‘stitching’ is applied as above, and in order to improve the image quality, a 3×3 median filter was applied to each step of Z_{12} , Z_{123} , and $Z_{12\cdots 4}$. The noise level, measured over a small smooth area of the coin surface, is reduced from $\delta Z_{12} = 385.0\,\mu\text{m}$ to $\delta Z_{14} = 3.8\,\mu\text{m}$. It is seen that final processed images with just a few micrometer noise is achieved with relatively mild application of median filters.

The process of MADH is illustrated with an example in Fig. 5, 6, where the object consists of a set of three mirror-like surfaces with nominal step heights 1.54 mm and 0.94 mm between them. A set of eight holograms are acquired, using a single HeNe laser of $\lambda_0 = 0.632\,8\,\mu\text{m}$, at illumination angles $\theta_n = \theta_0 + \Delta_n$, tabulated in Table 2. In this experiment, an alternate version of the optical apparatus was used, where the reference beam is stationary and only the object illumination is scanned. The starting position $\theta_0 = 18^\circ$ corresponds to the case of the object beam coinciding with the reference beam direction, while Δ_n are precisely controlled by the rotation stage with $0.000\,25^\circ$ resolution. The first two phase profiles Φ_1 and Φ_2 are displayed in Fig. 5a, b. The patterns indicate slight relative tilt between the three surfaces. The angular step $\theta_2 - \theta_1 = 0.0014^\circ$ between the first two holograms determines the synthetic wavelength $\Lambda_{12} = 7\,545\,\mu\text{m}$, with the effective wavelengths $\lambda_n = \lambda_0 \cos \theta_n = 0.601\,829\,\mu\text{m}$ and $0.601\,781\,\mu\text{m}$, for $n = 1$ and 2 , respectively. Additional

angular steps $\theta_n - \theta_1$, which increase by a factor of two in each step in this example, lead to synthetic wavelengths Λ_{1n} that decrease by a factor of $\alpha \approx 0.50$, each step for $n > 2$. The ‘stitching’ process is iterably applied with the series of profiles Z_{13}, \dots, Z_{18} . The noise levels δ_{1n} of the ‘stitched’ maps $Z_{12\cdots n}$, in Fig. 5, 6 are measured as the

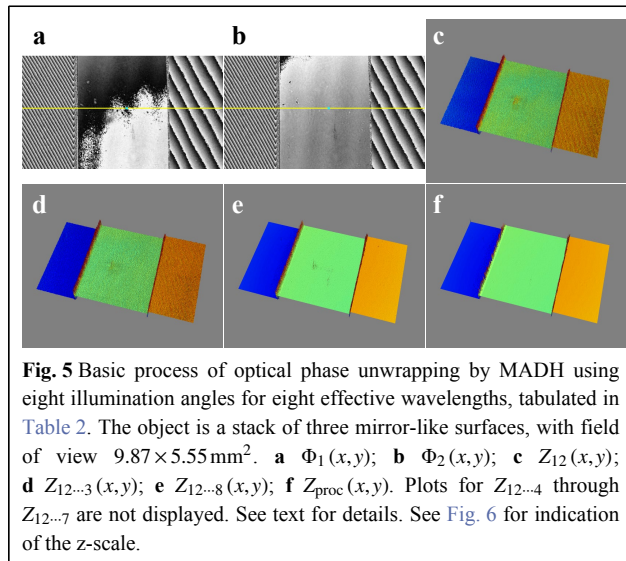
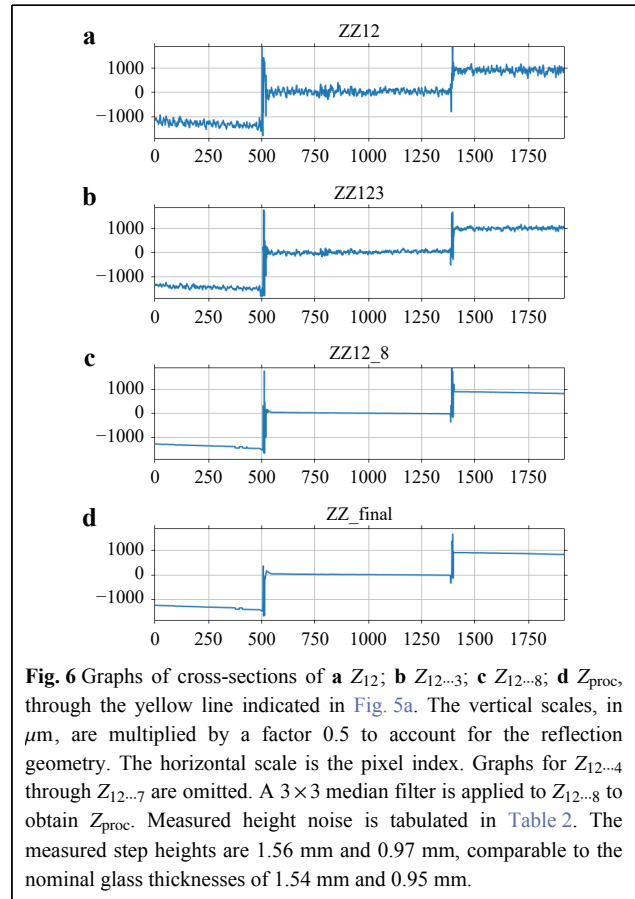


Table 2 Parameter used in Fig. 5. λ_n : individual wavelength; Δ_{1n} : difference wavelength; Λ_{1n} : synthetic wavelength; δZ_{1n} : noise in Z_{1n} ; ‘proc’: final processed profile.

n	$\lambda_n, \mu\text{m}$	$\Delta_{1n}, \mu\text{m}$	$\Lambda_{1n}, \mu\text{m}$	$\delta Z_{1n}, \mu\text{m}$
1	0.601 829			
2	0.601 781	0.000 048	7 545.193	127.426
3	0.601 733	0.000 096	3 772.296	76.897
4	0.601 637	0.000 192	1 885.847	35.985
5	0.601 445	0.000 384	942.623	20.029
6	0.601 060	0.000 769	470.397	6.961
7	0.600 281	0.001 548	233.376	4.057
8	0.598 697	0.003 132	115.043	3.507
proc				2.018

standard deviation of a small area near the center of the frame. They progressively decrease by a factor close to α each step, while maintaining the overall height range Λ_{12} . The surface profiles rendered as 3D plots in Figs. 5c–f show obvious enhancement of image quality between Z_{12} and $Z_{12\cdots 8}$, as the noise decreases from $\delta Z_{12} = 127.4 \mu\text{m}$ to $\delta Z_{18} = 3.5 \mu\text{m}$, with $\delta Z_{18}/\delta Z_{12} = 0.0275 = \alpha^{5.18}$, consistent with the expected factor of α^{n-2} . In this case, the noise reduction is quite complete throughout the surface except at the steps because of the beveled edges reflecting insufficient light towards the camera. With application of a mild 3×3 median filter on the last stitched profile $Z_{12\cdots 8}$, a final noise level of $\delta Z_{\text{proc}} = 2.0 \mu\text{m}$ is achieved over a height range of $\Lambda_{12} = 3758 \mu\text{m}$.

Fig. 7, 8 is an example surface profile of a coin (U.S. penny) placed on another (U.S. quarter). Here a set of eight holograms are acquired using the stepping factor $\alpha = 0.50$ for the synthetic wavelengths ranging from $\Lambda_{12} = 2911.5 \mu\text{m}$ to $\Lambda_{18} = 44.1 \mu\text{m}$. Because of the microscopically diffuse surface of the coin, as well as the slopes on the boundaries of the letters and relief features, there is significant noise in the raw profile Z_{12} , shown in Fig. 7c, 8a. The relatively small numerical aperture of the system, approx. 0.1, is not able to collect enough light from these sloped boundary surfaces for accurate phase information. The same stitching procedure as above is applied using the series Z_{13}, \dots, Z_{18} , but after each step a 3×3 median filter is applied. This produced reasonably clean surface profile of the coin without noticeable degradation or loss of lateral resolution. The measured noise reduced from $\delta Z_{12} = 147.3 \mu\text{m}$ to $\delta Z_{18} = 10.4 \mu\text{m}$.

As described in Section 4, there is a limit on how fast the iterative noise reduction can progress, i.e. how small the stepping factor α can be. For larger amount of initial noise,

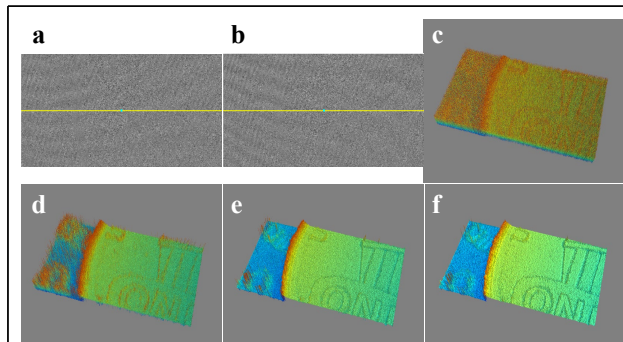


Fig. 7 Example of optical phase unwrapping by MADH. The object is a coin, US penny, placed on top of another, a US quarter, with field of view $9.87 \times 5.55 \text{ mm}^2$. A set of eight wavelengths are used, such that $\Lambda_{1n} = [2911.5, 1455.5, 727.5, 363.5, 180.9, 89.7, 44.1] \mu\text{m}$ for $n = 2, 3, \dots, 8$. **a** $\Phi_1(x, y)$; **b** $\Phi_2(x, y)$; **c** $Z_{12}(x, y)$; **d** $Z_{12\cdots 3}(x, y)$; **e** $Z_{12\cdots 8}(x, y)$; **f** $Z_{\text{proc}}(x, y)$. See Fig. 8 for indication of the z-scale.

the stepping factor cannot be chosen too small, for otherwise the iterative noise reduction can become incomplete. To illustrate, in Fig. 9, the same coin surface data as in Fig. 8 is used, but instead of stitching all of the profiles Z_{13}, \dots, Z_{18} on to Z_{12} , only the partial set of Z_{12}, Z_{15} , and Z_{18} is used for stitching. Here, $Z(12)$, $Z(12+15)$, and $Z(12+15+18)$, denote Z_{12} , it stitched with Z_{15} , and the last stitched with Z_{18} , respectively. This in effect reduces the stepping factor to $\alpha = 0.125$. Otherwise the same set of processing procedure is applied as with Fig. 8, including the 3×3 median filter at each stitching step. The stepping factor is too small and the iteration is too fast, and significant amount of noise escapes the reduction procedure, the final noise level being $34 \mu\text{m}$ for $\alpha = 0.125$, compared to $9.0 \mu\text{m}$ for $\alpha = 0.50$.

A few more examples of surface profiles are given in Fig. 10, by optical phase unwrapping with MWDH or MADH. Imaging parameters of the examples are summarized in Table 3.

Discussion

The median filter is quite effective in removing the spiky noise. For some of the examples presented in Section 2, such as coin surfaces, application of simple 3×3 median

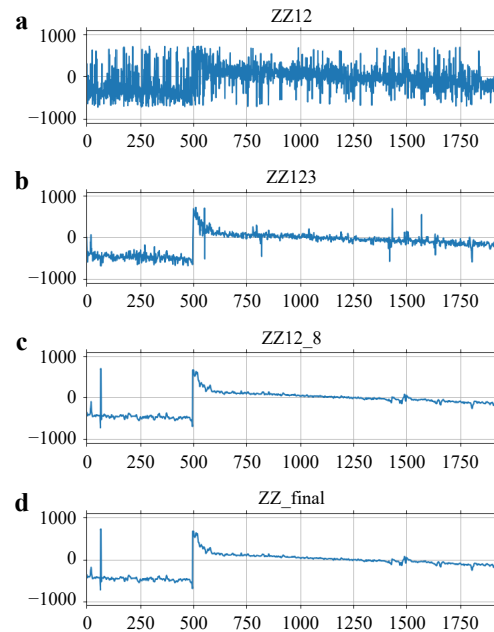


Fig. 8 Graphs of cross-sections of **a** Z_{12} ; **b** $Z_{12\cdots 3}$; **c** $Z_{12\cdots 8}$; **d** Z_{proc} , through the yellow line indicated in Fig. 7a. The vertical scales, in μm , are multiplied by a factor 0.5 to account for the reflection geometry. The horizontal scale is the pixel index. A 3×3 median filter is applied to each of $Z_{12} \sim Z_{12\cdots 8}$ and to Z_{proc} . Measured height noise varies as $\delta Z_{12\cdots n} = [147.3, 29.5, 27.2, 23.2, 15.5, 13.9, 10.4] \mu\text{m}$ for $n = 2, 3, \dots, 8$, and $\delta Z_{\text{proc}} = 9.0 \mu\text{m}$.

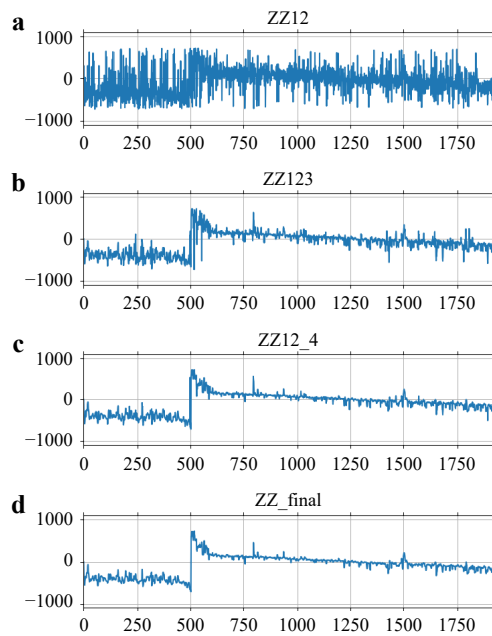


Fig. 9 Effect of iteration being too rapid with $\alpha = 0.125$. Graphs of cross-sections of **a** $Z(12)$; **b** $Z(12 + 15)$; **c** $Z(12 + 15 + 18)$; **d** Z_{proc} . The vertical scales, in μm , are multiplied by a factor 0.5 to account for the reflection geometry. The horizontal scale is the pixel index. A 3×3 median filter is applied to each profile. Measured height noise varies as $\delta Z_{12} = 147.3 \mu\text{m}$, $\delta Z_{12+15} = 58.7 \mu\text{m}$, $\delta Z_{12+18} = 42.2 \mu\text{m}$, and $\delta Z_{\text{proc}} = 34.1 \mu\text{m}$. See text for details.

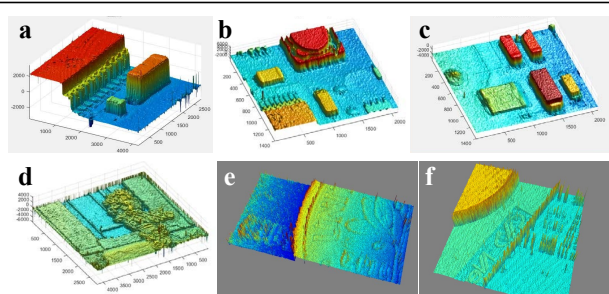


Fig. 10 Examples of MWDH and MADH images. Imaging parameters are tabulated in Table 3.

filter a few times was sufficient to produce good-quality surface profiles. For more rough textured surfaces such as integrated circuit chips and printed circuit boards, heavier dose of filtering was necessary, such as $10 \sim 20 \times$ repeated applications of 3×3 median filter. Some loss of surface details is inevitable, but it seems to be justified by the improvement in overall quality of the final image. It is also found useful in some cases to adjust the median filter to larger window size for darker areas of the amplitude image, and vice versa. Such adaptive median filter (AMF) technique was used to obtain the images in Figs. 10a–c, and helped reduce strong noise in corners and metallic electrodes.

Several other denoising methods were attempted from collection of ‘conventional’ image processing tools, such as windowed Fourier transform (WFT), total variation denoising (TVD), non-local means filtering (NLMF), and block-matching and 3D filtering (BM3D)¹⁸, as well as random mask multi-look (RMML) method for holographic speckle processing¹⁹. These somewhat casual studies did not find a magic solution for general applications, but each technique tends to be applicable only to specific cases, pose substantial computational load, and cause significant degradation of details. The behavior of spiky noise in this type of stitched phase maps appear very different from typical noise in photographic images or the speckle noise in holographic intensity images. Further systematic study of the behavior of this new type of noise may be of interest²⁰.

A few points can be made in comparing the methods of MWDH and MADH. First, both methods, when properly set up and carried out, can produce good quality surface profile images. In general, the MADH system has advantage with cost and complexity. The selection of effective wavelengths is very flexible and more controllable. A potential issue is shadowing and obscuration by tall or sharp surface features. The MWDH may be subject to chromatic aberration when the wavelength interval is substantial. The MADH can also be subject to geometric aberration because of the movement of the beam across the optical aperture. If the size of the

Table 3 Parameter used in Fig. 10. N_λ : number of wavelengths; Λ_{12} : first synthetic wavelength; Λ_{1N} : last synthetic wavelength.

Fig	object	method	N_λ	FOV, $\mu\text{m} \times \mu\text{m}$	Λ_{12} , μm	Λ_{1N} , μm
a	PCB	MWDH	4	30 500 \times 20 352	13 636.2	242.9
b	PCB	MWDH	4	21 200 \times 14 160	18 595.0	243.0
c	PCB	MWDH	4	21 200 \times 14 160	18 595.0	243.0
d	brass relief plaque	MWDH	4	30 500 \times 20 352	13 636.2	241.1
e	coin, US dime	MADH	8	9 870 \times 5 552	1 455.8	22.1
f	three mirror-like surfaces	MADH	4	18 432 \times 18 432	19 378.6	2 212.3

aberration is more than a few wavelengths, the reconstructed surface profile may include as much distortion. This type of distortion can be compensated for, if necessary, by acquiring a set of blank holograms with a flat mirror in place of the object plane.

There is an alternate approach to unwrapping of quantitative phase images by angular scanning, where small step phase changes are accumulated over many small step angular shifts²¹. General type and quality of surface profile images may be similar to the method presented here. In principle, in order to achieve the same level of height range and resolution, both methods of this paper and of²¹ start from the same first wavelength λ_1 and scan to the final synthetic wavelength λ_N . The method of²¹ takes uniform wavelength steps throughout the scan, while the method of this paper takes progressively larger steps to reach the final wavelength. Direct experimental comparison has not been attempted, but because of the significantly larger number of holographic frames, the acquisition may take longer time and therefore susceptible to instability.

One may also note other related but distinct holographic methods of surface profiling. For example, many holograms are acquired using a range of wavelengths. The stack of holograms is then Fourier transformed along the inverse-of-wavelength axis, which represents the 3D surface topography²². Similar result can be obtained by replacing the wavelength scanning with angular scanning^{23–25}. These processes in effect synthesize temporal incoherence from diversity of frequencies, i.e. inverse of wavelength, either by wavelength scanning or angular scanning. The axial resolution is limited by the synthesized coherence length and in principle significantly lower than the sub-wavelength axial resolution of phase profile-based methods presented here.

These demonstration experiments validate the basic concept of optical phase unwrapping and iterative noise reduction by multi-wavelength and multi-angle digital holography. With the quantitative phase method presented here, high resolution surface profiles can be obtained with large unambiguous range, while maintaining close to single-wavelength axial resolution. Further work is in progress, in particular with respect to the novel behavior of phase noise in this type of quantitative phase imaging system, as well as development of profilometry applications in device fabrication and biomedical imaging.

Materials and methods

Principle of optical phase unwrapping by MWDH

The basic process of multi-wavelength optical phase unwrapping is illustrated with simulations in Fig. 11.

Suppose the object is an inclined plane of height $a_h = 15 \mu\text{m}$, depicted with the function $h(x)$ in Fig. 11a, and a set of holograms are acquired using a series of wavelengths

$$\{\lambda_n\} = \lambda_1, \lambda_2, \lambda_3, \dots \quad (1)$$

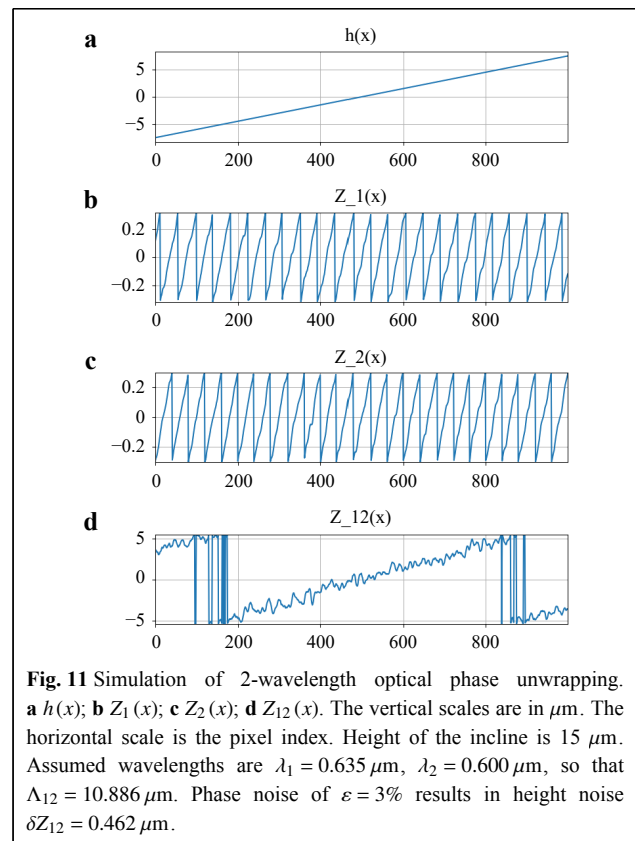
The complex optical fields

$$E_n(x, y) = a_n(x, y) \cdot \exp[i\Phi_n(x, y)] \quad (2)$$

are computed from the captured holographic interference patterns, where $a_n(x, y)$ and $\Phi_n(x, y)$ are the amplitude and phase profiles of the optical field, respectively. In off-axis holography, the phase is encoded as a modulation of the high-spatial-frequency interference fringe patterns in a single camera frame, whereas in phase-shifting digital holography, three or more camera frames are combined while the phase of reference field is shifted. If the acquired optical field resulted from reflection from or transmission through a structured surface or layer, the phase profile $\Phi_n(x, y)$ is directly proportional to the profile of the optical path length $Z(x, y)$

$$\Phi_n(x, y) = Z(x, y) \cdot \frac{2\pi}{\lambda_n} \quad (3)$$

The wrapped phase problem arises from the fact that the optical phase is defined only up to modulo 2π , and the



derived surface height profile

$$Z_n(x, y) = \Phi_n(x, y) \cdot \frac{\lambda_n}{2\pi} \quad (4)$$

is limited to modulo λ_n . In Fig. 11b the height profile Z_1 acquired using a wavelength $\lambda_1 = 0.635 \mu\text{m}$ has a sawtooth shape of height equal to the wavelength. A phase noise of standard deviation $2\pi \cdot \varepsilon$, with $\varepsilon = 3\%$, is added in the phase profile to simulate random phase noise between hologram acquisitions.

Two-wavelength optical phase unwrapping is based on taking the conjugate product of two optical fields acquired with two slightly different wavelengths, λ_1 and λ_2 , as

$$E_{12}(x, y) = E_1 \cdot E_2^* = a_{12} \cdot \exp[i\Phi_{12}(x, y)] \quad (5)$$

where

$$\Phi_{12} = \text{mod}(\Phi_1 - \Phi_2 + \pi, 2\pi) - \pi \quad (6)$$

The particular modulo operation is necessary when the phase angle of a complex number is defined in the range $[-\pi, \pi]$. The difference phase Φ_{12} is equivalent to the phase of an effective, or synthetic, wavelength Λ_{12} , which can be much larger than the original wavelengths:

$$\Phi_{12} = 2\pi \frac{Z}{\lambda_1} - 2\pi \frac{Z}{\lambda_2} = 2\pi \frac{Z}{\Lambda_{12}} \quad (7)$$

where

$$\Lambda_{12} = \frac{\lambda_1 \lambda_2}{|\lambda_1 - \lambda_2|} \quad (8)$$

The optical path derived from the difference phase can range up to the synthetic wavelength,

$$Z_{12}(x, y) = \Phi_{12} \cdot \frac{\Lambda_{12}}{2\pi} \quad (9)$$

as illustrated in Fig. 11d with $\lambda_1 = 0.6350 \mu\text{m}$ and $\lambda_2 = 0.6000 \mu\text{m}$, so that $\Lambda_{12} = 10.886 \mu\text{m}$, and the height profile $h(x)$ is properly represented up to the maximum Λ_{12} .

By choosing two closely spaced wavelengths λ_1 and λ_2 , the synthetic wavelength Λ_{12} can be made as large as necessary to cover the maximum surface height of the object to be profiled. On the other hand, the extension of the synthetic wavelength comes with amplification of noise in the height profile. For suppose the phase noise in Φ_1 is a fraction of 2π ,

$$\delta\Phi_n = 2\pi \cdot \varepsilon \quad (10)$$

where ε is a dimensionless random function that includes both spatial and frame-to-frame variations. The corresponding noise in the derived optical path is

$$\delta Z_n = \delta\Phi_n \cdot \frac{\lambda_n}{2\pi} = \varepsilon \cdot \lambda_n \quad (11)$$

which is approximately $\delta Z_1 = 0.019 \mu\text{m}$ with the assumed

values of $\lambda_1 = 0.635 \mu\text{m}$ and $\varepsilon = 3\%$. The noise in the optical height derived from the difference phase and synthetic wavelength is, with $\delta\Phi_{12} \approx \sqrt{2}\delta\Phi_1$,

$$\delta Z_{12} = \delta\Phi_{12} \cdot \frac{\Lambda_{12}}{2\pi} = \sqrt{2}\varepsilon \cdot \Lambda_{12} \quad (12)$$

and the noise in the optical height is amplified in proportion to the amplification in wavelength, to approx. $\delta Z_{12} \approx 0.462 \mu\text{m}$ in Fig. 11d. The amplification in wavelength is accompanied by similar amplification in noise.

The noise can be reduced if a shorter synthetic wavelength, Λ_{13} is used, with a larger difference $\lambda_1 - \lambda_3$. The simulation in Fig. 12 uses $\lambda_3 = 0.5300 \mu\text{m}$, so that $\Lambda_{13} = 3.205 \mu\text{m}$. Start from $Z_{12}(x, y)$ with the range $\Lambda_{12} = 10.886 \mu\text{m}$, Fig. 12a, and make integer steps of Λ_{13} , Fig. 12b. Then, ‘stitch’ the steps with the new profile $Z_{13}(x, y)$, Fig. 12c. That is,

$$Z_{12 \dots 3}(x, y) = \text{round}\left(\frac{Z_{12}(x, y)}{\Lambda_{13}}\right) \cdot \Lambda_{13} + Z_{13}(x, y) \quad (13)$$

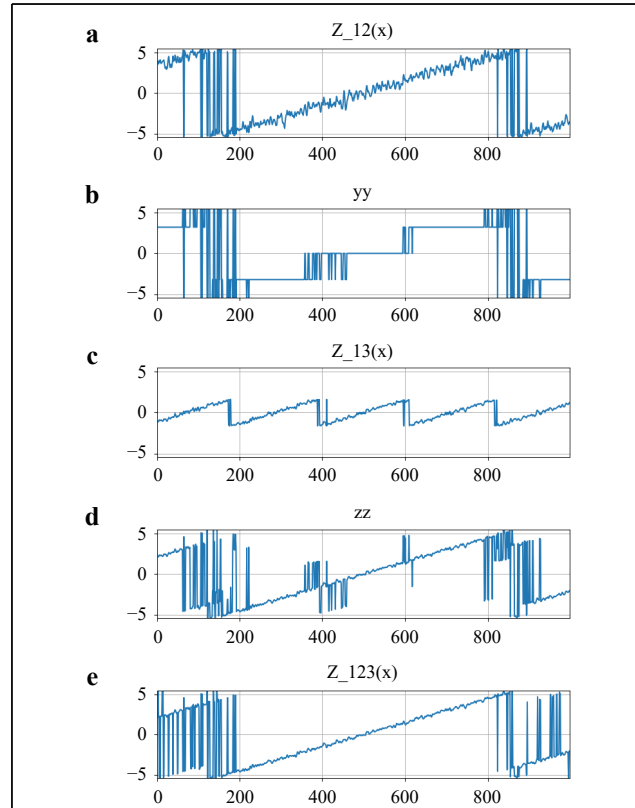


Fig. 12 Simulation of 3-wavelength optical phase unwrapping. **a** Z_{12} ; **b** $Y_{12} = \text{round}(Z_{12}/\Lambda_{13}) \cdot \Lambda_{13}$; **c** Z_{13} ; **d** $Z'_{12 \dots 3} = Y_{12} + Z_{13}$; **e** $Z_{12 \dots 3}$. The vertical scales are in μm . The horizontal scale is the pixel index. Assumed third wavelength is $\lambda_3 = 0.530 \mu\text{m}$, so that $\Lambda_{13} = 3.205 \mu\text{m}$. Final height noise is reduced to $\delta Z_{12 \dots 3} = 0.136 \mu\text{m}$.

where $\text{round}()$ represents integer rounding operation. If the phase noise is included in the above expression,

$$\begin{aligned} Z_{12\cdots 3} + \delta Z_{12\cdots 3} &= \text{round}\left(\frac{Z_{12} + \delta Z_{12\cdots 3}}{\Lambda_{13}}\right) \cdot \Lambda_{13} + (Z_{13} + \delta Z_{13}) \\ &= Z_{12\cdots 3} + \Delta \cdot \Lambda_{13} + \delta Z_{13} \\ &= Z_{12\cdots 3} + \Delta \cdot \Lambda_{13} + \sqrt{2}\varepsilon\Lambda_{13} \end{aligned} \quad (14)$$

Here $\Delta \cdot \Lambda_{13}$ represents spikes of height Λ_{13} scattered at positions near the step boundaries of $\text{round}()$, as evident in Fig. 12d. These spikes can be suppressed by adding or subtracting Λ_{13} wherever the absolute difference $|Z_{12} - Z_{12\cdots 3}|$ is comparable to Λ_{13} . This process is valid with the requirement

$$\frac{\delta Z_{12}}{\Lambda_{13}} \approx \sqrt{2}\varepsilon \cdot \frac{\Lambda_{12}}{\Lambda_{13}} \ll 1 \quad (15)$$

and Λ_{13} should be chosen large enough compared to $\sqrt{2}\varepsilon \cdot \Lambda_{12}$, or

$$\alpha = \Lambda_{13}/\Lambda_{12} \gg \sqrt{2}\varepsilon \quad (16)$$

The overall noise is then reduced from $\sqrt{2}\varepsilon \cdot \Lambda_{12} \approx 0.462 \mu\text{m}$ to $\sqrt{2}\varepsilon \cdot \Lambda_{13} \approx 0.136 \mu\text{m}$, as demonstrated in Fig. 12e.

In the above simulation example, the synthetic wavelength is extended to over $10 \mu\text{m}$, which can be suitable for profiling microscopically structured surfaces. On the other hand, for applications requiring profiling of macroscopic surfaces with millimeters of height range, the large amplification of wavelength entails similarly large noise. In order to reduce the large noise, it is then necessary to extend the iterative series using a larger number of wavelengths. Thus, another difference phase profile $\Phi_{14}(x, y)$ with synthetic wavelength $\Lambda_{14} < \Lambda_{13}$ is used to ‘stitch’ the new profile $Z_{14}(x, y)$ on to the previous synthesized profile $Z_{12\cdots 3}(x, y)$. If we again let $\Lambda_{14} = \alpha\Lambda_{13}$, the noise level for the new profile $Z_{12\cdots 4}$ is $\delta Z_{12\cdots 4} = \sqrt{2}\varepsilon\Lambda_{14} = \sqrt{2}\varepsilon \cdot \alpha^2\Lambda_{12}$. The process can continue until $\delta Z_{12\cdots n} = \varepsilon \cdot \Lambda_{1n} = \varepsilon \cdot \alpha^{(n-2)}\Lambda_{12}$ reaches desired height resolution. In the simulation of Fig. 13, the height range is now $\Lambda_{12} = 2000.0 \mu\text{m}$ with $\lambda_1 = 0.635000 \mu\text{m}$ and $\lambda_2 = 0.634798 \mu\text{m}$, or $\Delta_{12} = \lambda_1 - \lambda_2 = 0.000202 \mu\text{m}$. Three more wavelengths are used with difference wavelengths $\Delta_{13} = 0.000805 \mu\text{m}$, $\Delta_{14} = 0.003209 \mu\text{m}$, and $\Delta_{15} = 0.012646 \mu\text{m}$ for synthetic wavelengths $\Lambda_{13} = 500.0 \mu\text{m}$, $\Lambda_{14} = 125.0 \mu\text{m}$, and $\Lambda_{15} = 31.25 \mu\text{m}$, respectively, with a fixed stepping factor $\alpha = 0.25$ for the series. Assuming phase noise with $\varepsilon = 3\%$, the initial noise $84.9 \mu\text{m}$ in Z_{12} is progressively reduced to $21.2 \mu\text{m}$, $5.3 \mu\text{m}$, and $1.3 \mu\text{m}$ in Z_{13} , Z_{14} , and Z_{15} , respectively.

If the iteration is made to run too fast with the stepping factor α too small, the noise reduction by stitching as

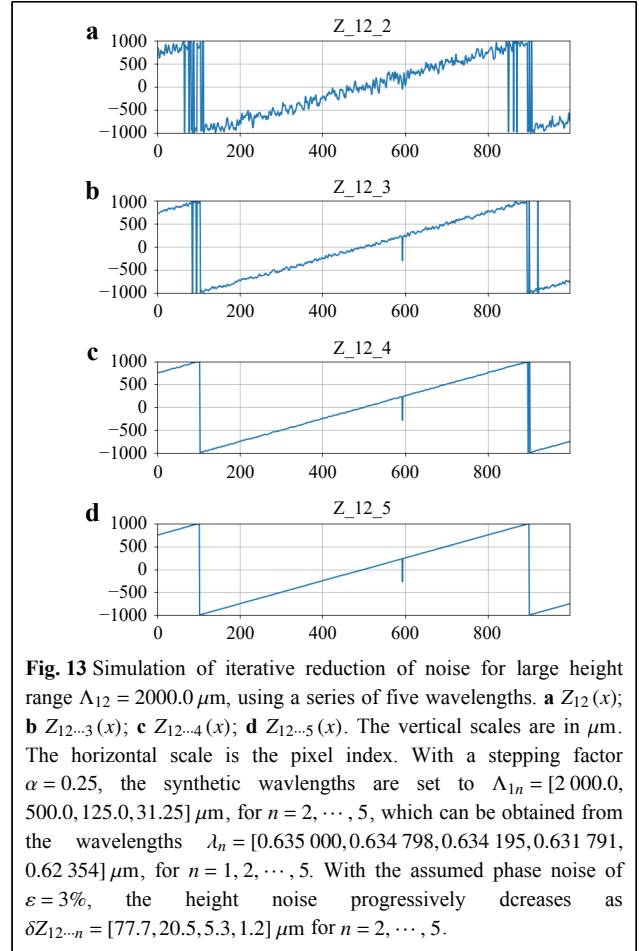


Fig. 13 Simulation of iterative reduction of noise for large height range $\Lambda_{12} = 2000.0 \mu\text{m}$, using a series of five wavelengths. **a** $Z_{12}(x)$; **b** $Z_{12\cdots 3}(x)$; **c** $Z_{12\cdots 4}(x)$; **d** $Z_{12\cdots 5}(x)$. The vertical scales are in μm . The horizontal scale is the pixel index. With a stepping factor $\alpha = 0.25$, the synthetic wavelengths are set to $\Lambda_{1n} = [2000.0, 500.0, 125.0, 31.25] \mu\text{m}$, for $n = 2, \dots, 5$, which can be obtained from the wavelengths $\lambda_n = [0.635000, 0.634798, 0.634195, 0.631791, 0.62354] \mu\text{m}$, for $n = 1, 2, \dots, 5$. With the assumed phase noise of $\varepsilon = 3\%$, the height noise progressively decreases as $\delta Z_{12\cdots n} = [77.7, 20.5, 5.3, 1.2] \mu\text{m}$ for $n = 2, \dots, 5$.

described above can be incomplete and significant amount of noise can remain after the procedure. In Fig. 14a, the noise is increased to $\varepsilon = 7\%$ while using the same set of wavelengths $\lambda_1, \dots, \lambda_5$, with $\alpha = 0.25$, as the above example. The condition $\varepsilon \ll \alpha$ is not sufficiently strong that there are many spikes $\Delta \cdot \Lambda_{1n}$ in resulting profiles $Z_{12\cdots n}$. In order to improve the noise figure, we slow the iteration using a larger value of $\alpha = 0.50$, and increase the number of wavelengths to eight, so that the final synthetic wavelengths in the two series are the same: $\Lambda_{18} = 31.25 \mu\text{m}$ with $\alpha = 0.25$ and $\Lambda_{15} = 31.25 \mu\text{m}$ with $\alpha = 0.50$. In Fig. 14b, the stitching process is applied to the series of eight wavelengths to obtain the profiles $Z_{12}, Z_{12\cdots 3}, \dots, Z_{12\cdots 8}$. The final noise level close to $\delta Z_{12\cdots 8} = 2.19 \mu\text{m}$ is achieved without significant number of spike. This simulation result suggests that large height or noisy surfaces may be profiled using slower progression of Λ_{1n} , i.e. larger α , and larger number of wavelengths.

The ‘stitching’ process is rather sensitive to a few different types of errors and these need to be addressed carefully. The process requires that each of the phase

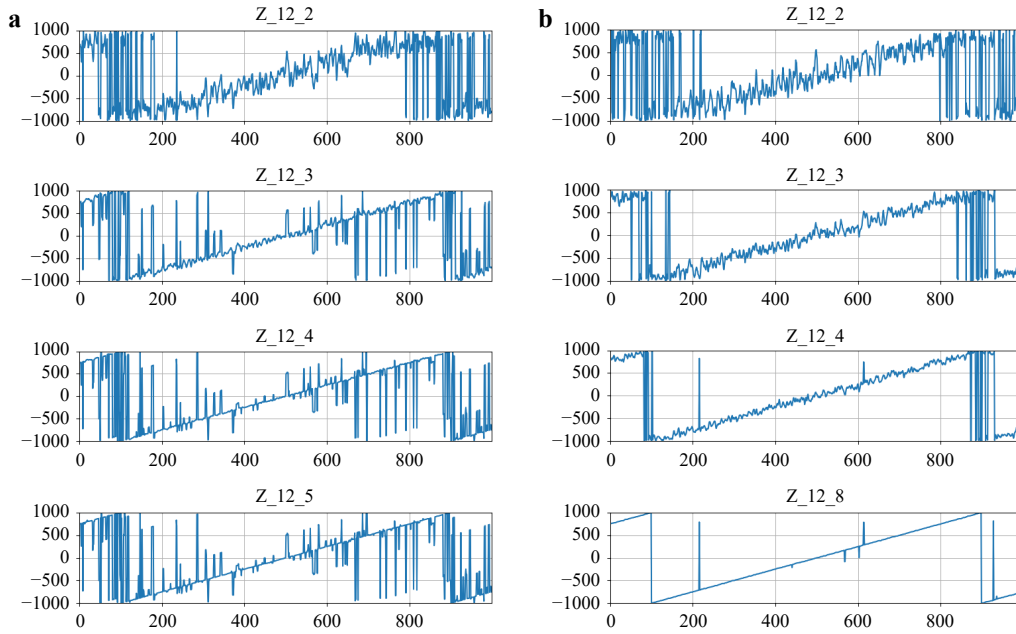


Fig. 14 Effect of stepping factor α for large noise profiles, with $\varepsilon = 7\%$. For the column **a**, the same stepping factor $\alpha = 0.25$ is used as in Fig. 13. The measured height noise is $\delta Z_{12 \dots n} = [110.0, 37.2, 51.6, 50.6] \mu\text{m}$ for $n = 2, \dots, 5$. For the column **b**, a slower stepping factor $\alpha = 0.50$ is used with eight wavelengths, so that the final synthetic wavelength $\Lambda_{18} = 31.25 \mu\text{m}$ is the same as Λ_{15} in **a**). Graphs for $Z_{12 \dots 5} \sim Z_{12 \dots 7}$ are omitted. The vertical scales are in μm . The horizontal scale is the pixel index. Now, the measured height noise is $\delta Z_{12 \dots n} = [99.2, 51.5, 35.5, 13.8, 11.5, 2.9, 2.2] \mu\text{m}$ for $n = 2, \dots, 8$. That is, the final noise value of $\delta Z_{12 \dots 8} = 2.2 \mu\text{m}$ obtains for $\alpha = 0.50$, instead of $\delta Z_{12 \dots 5} = 50.6 \mu\text{m}$ for $\alpha = 0.25$.

profiles $\Phi_n(x, y)$ is referenced to an identical global phase, which is never the case due to random variations in the laser, optical, and mechanical systems. This is remedied by fixing the difference phase $\Phi_{1n}(x_0, y_0)$ at a suitable, relatively noise-free, reference point to be zero.

Another source of error is that the synthetic wavelength is inversely proportionale to a small difference wavelength. In MWDH, the laser wavelengths drift with temperature and other factors. Although a high precision wave meter is available, the current setup does not incorporate tight monitoring and control of it. In MADH, the angular position is more closely monitored but the precision is limited and any mechanical instability may affect it. In any case, at least in the current setup, it is necessary, during post-processing, to verify and adjust the accuracy of synthetic wavelengths. This is carried out by scanning the synthetic wavelength over a range and looking for optimal values for minimizing the noise spikes.

Principle of optical phase unwrapping by MADH

For example, to achieve a height range of $\Lambda_{12} = 2.0 \text{ mm}$ near $\lambda = 0.635 \mu\text{m}$, the required wavelength difference is $\Delta\lambda \approx 0.2 \text{ nm}$. And to achieve μm -level height resolution, several wavelengths are needed. For such applications, acquiring and maintaining multiple laser sources with

precision-tuned wavelengths quickly becomes prohibitively difficult. The cost and complexity of the optical system can be significantly reduced if, instead of multiple lasers, a single laser is used and the multiple effective wavelengths are generated by changing the illumination angle of the object. The variation of the optical phase through a given height h of the object is $2\pi h / \lambda \cos \theta$, which can be described as illumination from a fixed direction with effective wavelength

$$\lambda_\theta = \lambda \cdot \cos \theta \quad (17)$$

Multiple effective wavelengths λ_n can be generated simply by tuning the illumination angle to various positions θ_n . The synthetic wavelength between the 1st and n -th effective wavelengths is then

$$\Lambda_{1n} = \frac{\lambda_1 \lambda_n}{|\lambda_1 - \lambda_n|} = \lambda \cdot \frac{\cos \theta_1 \cos \theta_n}{|\cos \theta_1 - \cos \theta_n|} \approx \lambda \cdot \frac{\cos \theta_1 \cos \theta_n}{\Delta \theta \cdot \sin \theta} \quad (18)$$

The rest of the theoretical description of MADH is in exact parallel with that of MWDH, but there are significant differences in practical considerations of the two methods. The MWDH requires multiple lasers or tunable lasers as well as a means to combine and switch between them, whereas the MADH requires one good laser and a means for fine control of illumination angle. To achieve 2.0 mm height range as above, the required angle shift is

$\Delta\theta = 0.070^\circ$, when $\theta = 15^\circ$, indicating the level of angular precision needed. The MADH is mostly immune from chromatic aberration but can be affected by spherical or higher order geometric aberrations due to the movement of the illumination across optical apertures. In order to keep Λ_{in} becoming too large, or the angular step $\Delta\theta$ too small, the angle θ needs to be somewhat away from zero, $\theta \sim 15^\circ$ for example. This can cause shadowing or obscuration of the object surface when the surface has sharp or tall features.

Optical system

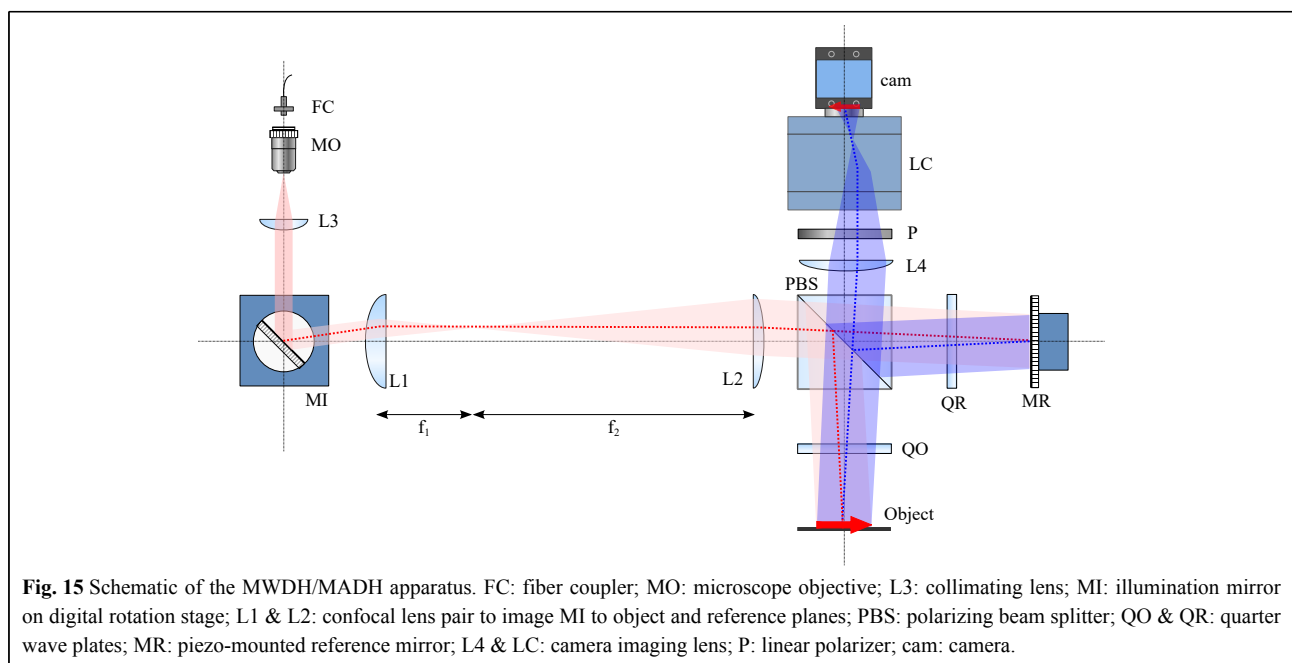
A schematic of one version of the optical system is depicted in Fig. 15, based on Michelson interferometer configuration. It can accommodate several operating modes, including multi-wavelength or multi-angle holography, as well as off-axis or phase-shifting holography. The fiber coupler FC introduces laser light into the system. Typical power input at FC is a few mW. Expanded and collimated beam is reflected by the mirror MI. The confocal lens combination L1 ($f_1 = 100$ mm) and L2 ($f_2 = 200$ mm) images the rotating mirror to the object plane, which is in turn imaged on to the camera plane by the lens L4 and a camera lens LC. The reference mirror MR is also conjugate with the camera plane, and is mounted on a piezo actuator for phase shifting. The polarizing beam-splitter PBS and quarter wave plates QO and QR together with the polarizer P controls and optimizes intensity ratio between the object and reference beams. The lenses L2 and L4 and quarter wave plates and

polarizer, as well as the polarizing beam splitter are 2 inches in diameter or width. Typical field of view of the object plane is 10 ~ 30 mm.

For multi-wavelength experiments, a set of four lasers (Lasos DPSS) are used with nominal wavelengths $\lambda_1 = 639.617$ nm, $\lambda_2 = 639.592$ nm, $\lambda_3 = 639.416$ nm, and $\lambda_4 = 637.928$ nm. These lasers are fiber-coupled into a four-channel fiber switch (Leoni), before being coupled into the interferometer. All fibers are polarization preserving single mode. The laser wavelengths do drift with changing temperature, and a high finesse wavemeter (Toptica) with 0.1 pm resolution was used to measure the wavelengths in real time before calculating synthetic wavelengths and other parameters.

For multi-angle experiments, a 30 mW HeNe laser fiber-coupled into the interferometer is deflected by the illumination mirror MI mounted on a motorized rotation stage (Thorlabs DDR25), which has encoder resolution of 0.000 25 deg/count. The starting angle $\theta_0 = 18^\circ$ is set with manual estimate using a ruler. Instead of trying to measure this angle with any better precision, the synthetic wavelength can be calibrated according to the known step size of an object. By placing both the object and reference planes conjugate to the camera, it is ensured that the relative angle of incidence between the two beams does not change with the rotation of the mirror.

In another configuration, based on a modified Mach-Zehnder interferometer, only the object beam is tilted while the reference beam remains stationary. This produces a slope in the holographic phase profile, but can be easily



compensated for numerically in reconstruction. The reference mirror MR can be tilted by an appropriate amount for off-axis digital holography, or piezo-shifted for phase-shifting digital holography.

Typically, a complex-valued hologram is acquired by combining several camera frames of interference intensity while the reference mirror is piezo-shifted, per standard procedures of phase-shifting digital holography. Then the source wavelength is switched in MWDH or the MI mirror angle is switched in MADH. A series of such holograms are acquired, which are then post-processed to construct the 3D surface profile of the object. Python-based programs are used for most of hardware control, image acquisition, and holographic image processing. Some parts of the software system also use LabVIEW and Matlab.

Acknowledgements

This project has not been externally funded.

Conflict of interest

The author declares no conflicts of interest.

Received: 17 September 2021 Revised: 08 February 2022 Accepted: 18 February 2022

Accepted article preview online: 08 March 2022

Published online: 06 May 2022

References

1. Stout, K. J. & Blunt, L. Three Dimensional Surface Topography. (London: Penton Press, 2000).
2. Cucho, E., Bevilacqua, F. & Depeursinge, C. Digital holography for quantitative phase-contrast imaging. *Optics Letters* **24**, 291-293 (1999).
3. Mann, C. J., et al. High-resolution quantitative phase-contrast microscopy by digital holography. *Optics Express* **13**, 8693-8698 (2005).
4. Marquet, P., Depeursinge, C. & Magistretti, P. J. Exploring neural cell dynamics with digital holographic microscopy. *Annual Review of Biomedical Engineering* **15**, 407-431 (2013).
5. Osten, W. Optical Inspection of Microsystems. (Boca Raton: Taylor & Francis, 2007).
6. Merola, F., et al. Tomographic flow cytometry by digital holography. *Light: Science & Applications* **6**, e16241 (2017).
7. Kim, M. K. Digital Holographic Microscopy. (New York: Springer, 2011).
8. Ghiglia, D. C. & Pritt, M. D. Two-Dimensional Phase Unwrapping: Theory, Algorithms, and Software. (New York: Wiley, 1998).
9. Gass, J., Dakoff, A. & Kim, M. K. Phase imaging without 2π ambiguity by multiwavelength digital holograph. *Optics Letters* **28**, 1141-1143 (2003).
10. Parshall, D. & Kim, M. K. Digital holographic microscopy with dual-wavelength phase unwrapping. *Applied Optics* **45**, 451-459 (2006).
11. Khmaladze, A., et al. Simultaneous dual-wavelength reflection digital holography applied to the study of the porous coal samples. *Applied Optics* **47**, 3202-3210 (2008).
12. Cheng, Y. Y. & Wyant, J. C. Two-wavelength phase shifting interferometry. *Applied Optics* **23**, 4539-4543 (1984).
13. Wagner, C., Osten, W. & Seebacher, S. Direct shape measurement by digital wavefront reconstruction and multi-wavelength contouring. *Optical Engineering* **39**, 79-85 (2000).
14. Wada, A., Ka to, M. & Ishii, Y. Large step-height measurements using multiple-wavelength holographic interferometry with tunable laser diodes. *Journal of the Optical Society of America A* **25**, 3013-3020 (2008).
15. Mann, C. J., et al. Quantitative phase imaging by three-wavelength digital holography. *Optics Express* **16**, 9753-9764 (2008).
16. De Nicola, S., et al. Recovering correct phase information in multiwavelength digital holographic microscopy by compensation for chromatic aberrations. *Optics Letters* **30**, 2706-2708 (2005).
17. Yamaguchi, I., Oh ta, S. & Kato, J. I. Surface contouring by phase-shifting digital holography. *Optics and Lasers in Engineering* **36**, 417-428 (2001).
18. Gonzalez, R. C. & Woods, R. E. Digital Image Processing. 3rd edn. (Upper Saddle River: Pearson, 2016).
19. Bianco, V., et al. Quasi noise-free digital holography. *Light: Science & Applications* **5**, e16142 (2016).
20. Xia, H. T., et al. Phase calibration unwrapping algorithm for phase data corrupted by strong decorrelation speckle noise. *Optics Express* **24**, 28713-28730 (2016).
21. Psota, P., et al. Multiple angle digital holography for the shape measurement of the unpainted tympanic membrane. *Optics Express* **28**, 24614-24628 (2020).
22. Kim, M. K. Tomographic three-dimensional imaging of a biological specimen using wavelength-scanning digital interference holography. *Optics Express* **7**, 305-310 (2000).
23. Jeon, Y. & Hong, C. K. Optical section imaging of the tilted planes by illumination-angle-scanning digital interference holography. *Applied Optics* **49**, 5110-5116 (2010).
24. Dong, J., J ia, S. H. & Jiang, C. Surface shape measurement by multi-illumination lensless Fourier transform digital holographic interferometry. *Optics Communications* **402**, 91-96 (2017).
25. Martinez-Carranza, J., et al. Multi-incidence digital holographic profilometry with high axial resolution and enlarged measurement range. *Optics Express* **28**, 8185-8199 (2020).